Dynamic traction force measurements of migrating immune cells in 3D matrices

David Böhringer[1], Mar Cóndor[2], Lars Bischof[1], Tina Czerwinski[1], Andreas Bauer[1], Caroline Voskens[3], Silvia Budday[4], Christoph Mark[1], Ben Fabry[1] ✉, and Richard Gerum[1,5]

[1]Department of Physics, Friedrich-Alexander-Universität Erlangen-Nürnberg, Erlangen, Germany
[2]Life Sciences Technology Department, Interuniversity Micro-Electronics Centre, Leuven, Belgium
[3]Department of Dermatology, University Hospital Erlangen, Friedrich-Alexander-Universität Erlangen-Nürnberg, Erlangen, Germany
[4]Department of Mechanical Engineering, Friedrich-Alexander-Universität Erlangen-Nürnberg, Erlangen, Germany
[5]Department of Physics and Astronomy, York University, Toronto, Canada

Immune cells such as natural killer (NK) cells migrate with high speeds of several µm/min through dense tissue, but the traction forces are unknown. We present a method to measure dynamic traction forces of fast migrating cells in non-linear biopolymer matrices. We find that NK cells display bursts of large traction forces that increase with matrix stiffness and facilitate migration through tight constrictions.

Correspondence: ***ben.fabry@fau.de***

Essential cell functions such as migration and spreading require that cells exert traction forces on their extracellular matrix. Several traction force microscopy methods exist that measure the force-induced deformations of the extracellular matrix, and reconstruct the cell forces based on continuum-mechanical principles. Mathematically, the reconstruction problem is a so-called inverse problem, where small measurement noise can give rise to large erroneous forces. This is typically solved by various smoothing or force regularization methods (1–3). Nonetheless, for cells grown on two-dimensional (flat) matrices with linear elastic properties, such as polyacrylamide hydrogels or silicone elastomers, robust and computationally inexpensive methods have been developed (4–7). The force reconstruction problem becomes considerably more difficult in 3 dimensions, however, especially in the case of mechanically non-linear materials, such as collagen or fibrin hydrogels (8–14), which are frequently used as a 3-D matrix for cell culture.

Current 3-D force reconstruction methods typically require the recording of a large 3-D image stack around a cell that is sufficiently far away from other cells. In addition, knowledge of the cell surface (Fig. 1a top), where by definition the traction forces are located, is also required for most methods. Staining and 3-D imaging the cell surface, however, can affect cell behavior or cause photo-damage. All current methods require knowledge of the force-free reference configuration of the matrix, which is obtained either by detaching the cell from the matrix, by the addition of drugs that suppress cell forces (e.g. cytochalasin D), or by killing the cell, e.g., with high-intensity laser light (Fig. 1b top). Such methods therefore pose limitations for measuring traction forces of rapidly moving cells, such as immune cells, or for investigating multiple cells within a culture dish.

Here, we overcome these limitations by a locally adjusted regularization approach, and by obtaining the force-free reference configuration of the matrix from time-lapse images. Our method builds on a previously developed non-linear semi-affine network optimizer (Saeno) (15). This method iteratively minimizes the discrepancy between measured and reconstructed matrix deformations (Fig. 1a middle) by adjusting point forces that can appear anywhere in the volume but are regularized to favor few, large forces that are typically located near the cell body. Cell forces are then summed over a user-defined sphere around the cell (15, 16). One advantage of this approach is that the exact position of the cell surface does not need to be known. A disadvantage is that balancing forces from sources outside the image stack can occur throughout the reconstructed force field.

In our new Python-based implementation (Saenopy), we regularize the reconstructed forces only within the reconstruction volume (which can be of the same size as the image stack, or larger) but not at its boundaries. This ensures that balancing forces from sources outside the image stack appear only at the surface of the reconstruction volume. Therefore, we do not need to limit the reconstructed cell forces to be within a defined distance around the cell (15, 16) (Fig. 1a middle) and instead can integrate them over the entire reconstruction volume, excluding the surface. This allows the size of the imaged volume to be greatly reduced without losing accuracy (Fig. 1c). It is furthermore no longer required that the force-induced matrix deformations near the image stack boundary should tend to zero. Importantly, we image the cells for a sufficiently long time so that the cell has either migrated outside the image stack, or that the cell forces have changed their direction and magnitude multiple times so that the time average (median) of the matrix deformations corresponds to the undeformed state (Fig. 1b bottom).

Using computer simulations of force-generating dipoles or quadrupoles with cell-like dimensions (15–30 µm) and forces, we verify the linearity of our method over a large force range (2 nN–400 nN) even for highly non-linear matrices such as collagen (Fig. 1d), and confirm high sensitivity even in the presence of considerable imaging noise.

For a simulated cell that generates 20 nN (dipole) or 40 nN (quadrupole) of force, typical displacement noise level of our confocal microscope of around 100 nm (σ_x=41 nm, σ_y=42 nm, σ_z=99 nm) result in relative errors of contractility below 5% and relative errors of strain energy below 15%.

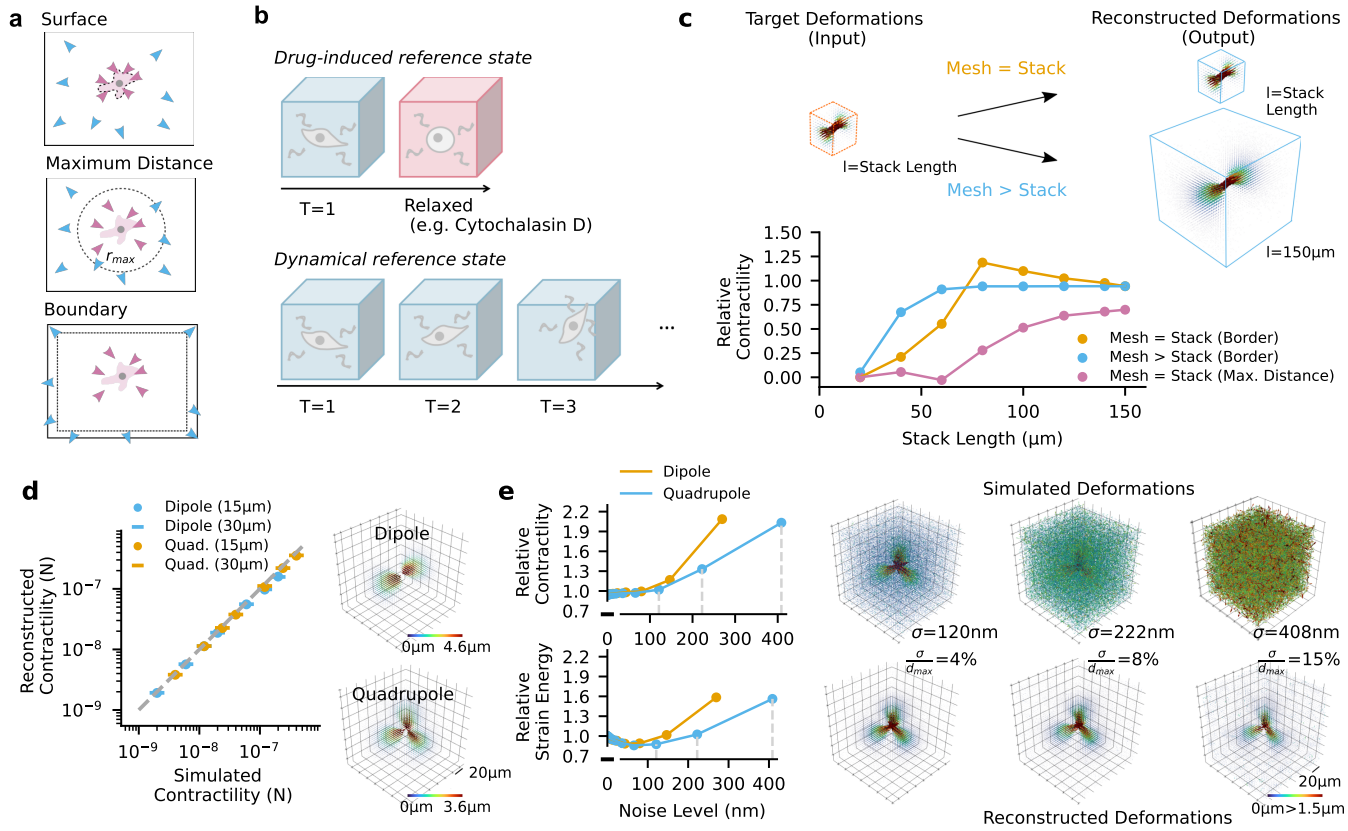

Fig. 1. Material model: **a**, Schematic of different regularization strategies. Top: Traction force microscopy (TFM) typically constrains forces (purple) to the cell surface. Middle: Body force microscopy with global regularization reconstructs forces without knowledge of the cell surface. Forces within a defined distance ($r_{\max}$) around the force epicenter are considered cell-generated forces (blue), forces beyond $r_{\max}$ (dotted gray line) are considered balancing forces (purple) to account for noise, drift, or contractile cells outside the field of view. Bottom: Saenopy is a body force microscopy method where forces are regularized throughout the image stack except for the boundary regions. This ensures that balancing forces appear only at the boundaries. **b**, Schematic of two methods for measuring the force-free matrix configuration. Top: Cell forces are relaxed using actin-depolymerizing or myosin-inhibiting drugs. 3D matrix deformations are measured from two image stacks recorded before and after drug treatment. Bottom: The force-free matrix configuration is computed from the cumulative matrix displacements between consecutive image stacks of a time series, median-averaged over the observation period. Dynamic 3D matrix deformations are obtained from the cumulative matrix displacements relative to the median average. **c**, Influence of image stack size and reconstruction volume on force reconstruction accuracy. The cell is simulated by a force dipole with 20 nN and a distance of 30 µm. The image stack size (cube length) is increased between (20 µm–150 µm)^3. The reconstruction volume (mesh) has either the same dimensions as the image stack (yellow) or has a constant size of (150 µm)^3 (blue). Force reconstruction is performed with Saenopy regularization (Fig. 1a bottom, yellow and blue lines) or with global regularization ($r_{\max}$ = 50 µm, Fig. 1a middle, magenta line). **d**, Accuracy of force reconstruction for simulated dipoles (upper inset) and quadrupoles (lower inset) for different contractilities. Dipoles or quadrupoles are simulated as pairs of monopoles either 15 µm or 30 µm apart. Contractility is the sum of the force monopoles. Dashed gray line shows line of identity. **e**, Influence of noise on force reconstruction (top) and strain energy (bottom) for simulated dipoles (contractility of 20 nN) or quadrupoles (contractility of 40 nN). Maximum matrix deformations are around 3 µm in both cases. Noise is added as Gaussian noise with specified standard deviation σ to the deformation field (upper right images for three selected noise values) and is expressed as absolute sd noise σ or percentage of sd noise relative to the maximum matrix deformations $\frac{\sigma}{d_{\max}}$. Lower right images show reconstructed deformation fields. Reconstructed contractility and strain energy are expressed relative to the input values.

Even for displacement errors up to 150 nm, both relative errors remain below 20 % (Fig. 1e).

We apply our method to measure traction forces of immune cells. Immune cells migrate in a so-called amoeboid mode with limited or no proteolytic activity and with limited or no specific (e.g. integrin-mediated) adhesion to the extracellular matrix (ECM) (17, 18). Therefore, it is thought that these cells do not generate substantial traction forces for migration. Here, we measure the force generation of natural killer cells (NK92 cell line) during migration in a 1.2 mg/ml collagen gel (shear modulus in the linear range of 100 Pa SI Fig. 1–2, average pore size 4.4 µm SI Fig. 3). We record one image stack (123×123×123 µm, voxel size 0.24×0.24×1 µm, acquisition time of 10 seconds using a resonance scanner (8000 Hz) and a galvo stage) every minute for 24 min. From these 24 image stacks, we estimate the force-free matrix configuration (undeformed reference state) from the median deformation averaged over the entire observation period (Fig. 1b). Cell forces at each time point are then computed from the current matrix deformations relative to the undeformed reference state using particle image velocimetry (19). Thus, this method allows for dynamic deformation measurements of highly motile cells with rapidly fluctuating traction forces. From the cell positions and cell shape, we also measure cell velocity and aspect ratio (Fig. 2a–c).

Around 78 % of the NK cells migrate by more than one cell diameter (13 µm) during the observation time of 24 min (SI Fig. 5 (we measure only cells that are elongated at t=0, which favors migratory cells). When migrating, NK cells show an elongated morphology, whereas non-migrating cells remain round. The majority of migrating cells show bursts of substantial contractile forces between 5–50 nN (Fig. 2d, SI Video 12–15), lasting typically 3–5 min, followed by non-contractile phases (< 5 nN). Cells migrate both during

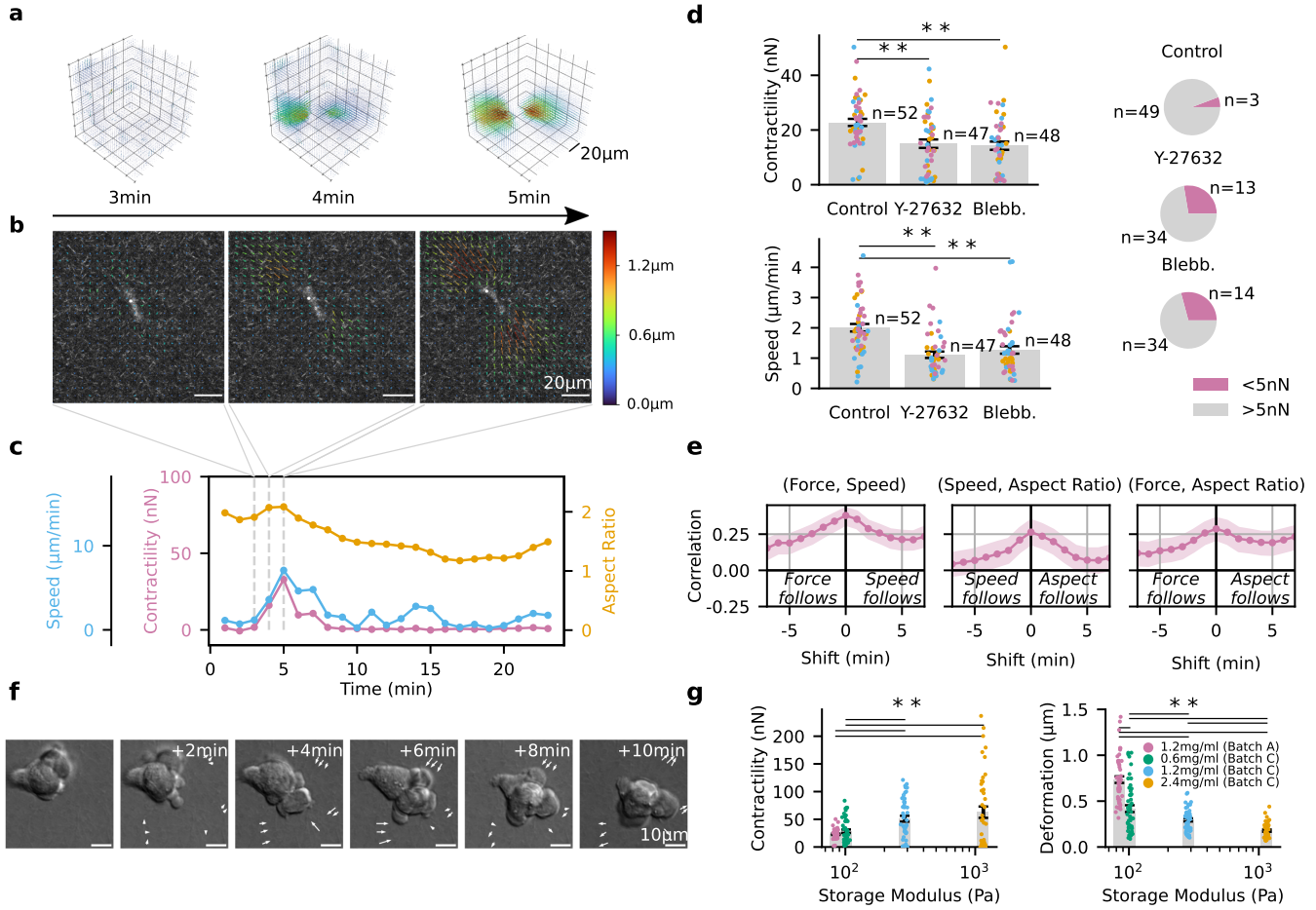

Fig. 2. Contractile phases during natural killer cell migration. **a**, Matrix deformations (relative to the dynamic reference state) around a natural killer cell migrating in a collagen type I hydrogel at 3 time points selected from a 24 min time series. **b**, Corresponding maximum-intensity projected confocal reflection image overlaid with the projected maximum matrix deformation field. **c**, Cell speed (blue), cell aspect ratio (1: round, >1: elongated, orange) and cell contractility (magenta) over a 24 min period. Dashed gray lines indicate the time points shown in Fig. 2a,b. **d**, Cells treated with Y-27632 (10 µM) or Blebbistatin (3 µM) show a decrease in maximum contractility (top left, mean±se), decrease in speed (bottom left, mean±se), and a decrease in the fraction of contractile cells (defined as contractility > 5 nN). Measurements of individual cells are shown as points, colors indicate independent experiments from different days. ** indicates p<0.01 for two-sided t-test. **e**, Cross-correlation between time courses of speed and force (left), speed and aspect ratio (middle), and aspect ratio and force (right). Signals were shifted relative to each other by ±5 min. The physical meaning of a positive correlation for different time points is indicated in the diagrams. Data points are mean values from 52 cells, shaded areas indicate one standard deviation determined by bootstrapping. **f**, Differential interference contrast (DIC) images show morphological changes of a NK cell during migration through collagen pores. Arrows indicate the local matrix deformation between consecutive frames. **g**, Cell contractility (maximum value within 24 min measurement period) and matrix deformation (99% percentile value of the absolute matrix deformation vectors is calculated per timestep. Then we choose the maximum value within 24 min measurement period) of NK92 cells embedded in collagen gels of different stiffness (mean±se for 44–56 cells from three independent experiments; ** indicates p<0.01 for two-sided t-test, SI Fig. 4). The storage modulus of different collagen gels in the linear regime is derived from shear rheological measurements with 1% strain amplitude and and a frequency of 0.02 Hz (SI Fig. 2).

contractile and non-contractile phases, but contractile phases were significantly ($p < 0.01$) correlated with higher speed and higher cell aspect ratio (Fig. 2c, e). Accordingly, speed and aspect ratio were also positively correlated (Fig. 2e). Myosin inhibition with blebbistatin and Rho-kinase inhibitor Y-27632 markedly reduced the magnitude and frequency of force bursts (Fig. 2d) and also reduced the migration speed (Fig. 2d).

Our discovery of substantial contractile forces in migrating immune cells that are approaching or even matching those of much larger cells, such as metastatic breast carcinoma cells (MDA-MB-231) or mouse embryonic fibroblasts (15, 20, 21), is surprising, as amoeboid migration is thought to be facilitated by shape changes and low frictional (traction) forces with the matrix (17, 18, 22). While our observation of long migratory phases with low tractions is in agreement with this notion, the occurrence of large traction force bursts points to a strong coupling of the cell's contractile machinery to the extracellular matrix during these brief phases. Such strong coupling may be essential for migration through small matrix pores that pose a high steric hindrance and require large cell shape changes (Fig. 2f, SI Video 12–15).

The idea of a strong coupling between the contractile machinery and the mechanical properties of the extracellular matrix in immune cells is supported by our finding of higher tractions in collagen gels with higher stiffness (Fig. 2g, SI Fig. 4). This behavior is reminiscent of mesenchymal cells that typically also respond with higher traction forces to higher matrix stiffness (10, 23, 24). In mesenchymal cells, this mechanosensitive behavior is facilitated by integrin-mediated cell adhesions with the matrix. Our finding of a similar mechanosensitive behavior in immune cells, together with our discov-

ery of traction force bursts that are comparable in magnitude to those generated by mesenchymal cells, suggest that strong integrin-mediated adhesions may also be involved in immune cell migration through tight constrictions.

In summary, our method allows for the dynamic measurement of 3-D traction forces in highly migratory cells over prolonged time periods, such as immune cells in a 3-D fiber network such as collagen, Matrigel or fibrin. The discovery of brief contractile phases of immune cells during migration in dense tissue has broad biological implications and adds to our current understanding of how immune cells migrate through tissue for their homing towards target sites in inflammation or cancer. The method can also be applied to slow migrating single cells and cell colonies, spheroids and organoids, although in these cases the force-free matrix configuration can usually not be obtained by time-averaging of the matrix deformations. For a user-friendly implementation of the method, we provide a Python-based graphical interface (SI Fig. 11).

Material and Methods

Material model. Our method uses a previously developed material model for biopolymer hydrogels (15, 25). The material is filled with isotropically oriented fibers, each exhibiting the same non-linear stiffness (ω'') versus strain (λ) relationship according to Eq. (1) (Fig. 3). In particular, for small extensional strain in the linear range ($0 < \lambda < \lambda_s$), fibers exhibit constant stiffness k. For compressive strain ($-1 < \lambda < 0$), fibers buckle and show an exponential decay of the stiffness with a characteristic buckling coefficient d_0. For larger extensional strain beyond the linear range ($\lambda_s < \lambda$), the fibers show strain stiffening with an exponential increase of stiffness with a characteristic stiffening coefficient d_s.

$$w''(\lambda) = \begin{cases} k \exp\left(\frac{\lambda}{d_0}\right) & \text{if } -1 \leq \lambda < 0 \text{ softening} \\ k & \text{if } 0 \leq \lambda < \lambda_s \text{ linear} \\ k \exp\left(\frac{\lambda - \lambda_s}{d_s}\right) & \text{if } \lambda_s \leq \lambda \text{ stiffening} \end{cases} \quad (1)$$

This description gives rise to a semi-affine behavior: Deformations cause non-affine deformations of the individual fibers, e.g. some fibers may buckle while others are stretched, depending on their orientation. Our material model approximates the contributions of individual fibers to the mechanical behavior of the material by using a mean-field approach. We approximate the material behavior by averaging over many isotropically oriented fibers so that all spatial directions contribute equally.

Specifically, the energy function $w(\lambda)$ is used to calculate the energy density W stored in the material for a given deformation gradient $\mathbf{F}$, averaged over the full solid angle Ω (15, 25):

$$W = \langle \omega(|\mathbf{F} \cdot \vec{e_r}(\Omega)| - 1) \rangle_\Omega \quad (2)$$

The strain λ of a unit vector $\vec{e_r}(\Omega)$ (representing a fiber), $\lambda = |\mathbf{F} \cdot \vec{e_r}(\Omega)| - 1$, is used to calculate the energy $\omega(\lambda)$ stored in this spatial direction. The strain is averaged over the full solid angle Ω, approximated by a finite set (typically 300) of homogeneously and isotropically distributed unit vectors $\vec{e_r}(\Omega)$.

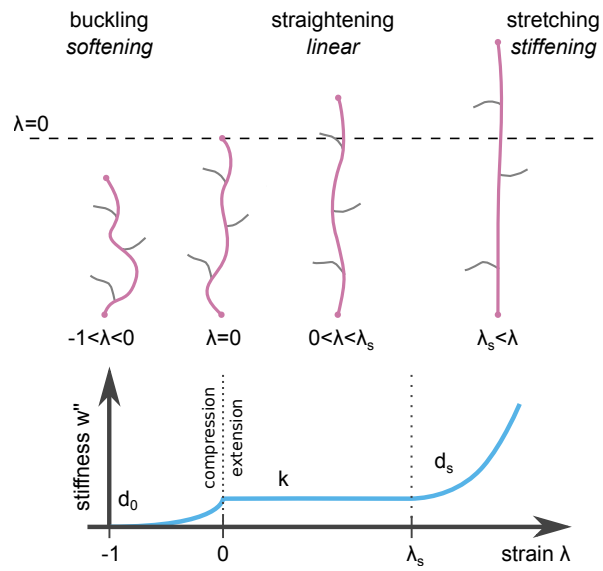

Fig. 3. The nonlinear material model divides the mechanical response of individual fibers into a region where fiber stiffness (ω'') decreases exponentially with decreasing strain under compression (buckling), a region of constant fiber stiffness for small strains (straightening), and a region of exponentially increasing fiber stiffness for larger strains (stretching) (15).

Finite element model. To describe the material behavior in the case of an inhomogenous deformation field, we tessellate the material volume into a mesh of linear tetrahedral elements T. The deformation field is then modeled as deformations $\vec{U}$ of the nodes of these elements. The total energy $E(\vec{U})$ of the mesh is the sum over the energy density W of all tetrahedral elements T multiplied by their volume V_T:

$$E(\vec{U}) = \sum_T W(\mathbf{F}(\vec{U})_T) \cdot V_T \quad (3)$$

From the total energy $E(\vec{U})$, we calculate the stiffness matrix $\mathbf{K}(\vec{U})$ and the nodal forces $\vec{f}(\vec{U})$ (15, 25):

$$\mathbf{K}_{ij}(\vec{U}) = \frac{\partial E(\vec{U})}{\partial \vec{U}_i \partial \vec{U}_j} \quad (4)$$

$$\vec{f}_i(\vec{U}) = \frac{\partial E(\vec{U})}{\partial \vec{U}_i} \quad (5)$$

Index i represents the nodes of the finite element mesh, with index j representing the adjacent nodes.

Mechanical characterization of biopolymer networks. Two different rheological experiments are performed to measure the macrorheological behaviour of collagen hydrogels. First, we use a cone-plate rheometer (Discovery HR-3, TA Instruments, Milford, 20 mm cone-plate geometry, 2° angle, truncation gap 54 µm) to measure the stress-strain relationship of collagen gels for simple shear deformation. The collagen sample (85 µl) is polymerized inside the rheometer setup

at 37°C for 30 min. A solvent trap filled with water is used to prevent evaporation and drying out of the sample. An initial frequency sweep (0.2 - 2 Hz) is performed at a low amplitude of 1%. Then, the stress-strain relationship is measured for a strain ramp from 0% to 100% with a constant strain rate of 1%/s.

In a second experiment, we measure the vertical contraction of collagen gels in response to horizontal uniaxial stretching. Stretching is performed using 2x2 cm flexible polydimethylsiloxane (PDMS) membranes (Sylgard184; crosslinker-to-base ratios of 1:14; cured for 24 h at 65°C, Sigma-Aldrich, St. Louis) as described in (26). The PDMS membrane is pre-stretched to 5% and coated with 0.5 mg/ml Sulfo-SANPAH (Thermo Fischer, Waltham) followed by 5 min UV treatment and 3x washing with phosphate buffered saline (Gibco PBS, Thermo Fischer, Waltham). Next, 700 µl of unpolymerized collagen solution is mixed with 4 µm silica beads (Kisker Biotech, Steinfurt) that serve as fiducial markers (5 µl beads per 1 ml). The collagen solution is transferred to the PDMS membrane, and after 20 min polymerization at 37°C and 5% CO_2, another 5 µl of the silica bead suspension is pipetted onto the gel to mark the gel surface. The collagen is polymerized for a total of 1 hour, after which 1 ml of DMEM Medium (1 g/l glucose, Thermo Fischer, Waltham) is added on top. The collagen gel is stretched uniaxially in 1% step increments using a custom made stepper-motor driven cell stretching device (27) mounted on an epifluorescence microscope (Leica DMI6000 CS equipped with a 20x Leica HCX PL Fluotator objective, Leica, Wetzlar). For each stretch increment, we measure the gel thickness by focusing on the top and bottom surface of the gel (highest and lowest layer of beads) and correct for the refractive index of water.

We investigate the influence of three different collagen batches and different collagen concentrations (0.6, 1.2 and 2.4 ml/ml) on the material behavior and the resulting material model parameters (SI Fig. 1). Because a cone-plate rheometer or uniaxial stretching device may not be available in every laboratory, and hence the correct material parameter for a given collagen batch may be unknown, we also quantify the effects of using erroneous material parameters on cellular force reconstruction. (SI Fig. 6-8). Furthermore, we explore the possibility to derive the linear stiffness parameter k_0 of the material model, which most sensitively affects force reconstruction, from oscillatory cone-plate rheology measurements in the linear range (SI Fig. 2).

Estimating material parameters from rheological measurements. As the material model is based on the mechanical behavior of microscopic biopolymer fibers, the model parameters cannot be directly extracted from macroscopic rheological measurements. Instead, we simulate the macro-rheological experiments using different model parameters until a best-fit is achieved (SI Fig. 1). Data from uniaxial stretching are required to fit the buckling coefficient d_0 of the material. For the other parameters, either data from a shear rheometery or an extensional rheometry experiment are sufficient as long as the strain range exceeds the linear range of the material (28).

Collagen gel preparation. Collagen type 1 hydrogels are prepared from acid-dissolved rat tail (R) and bovine skin (G1) collagen (Matrix Bioscience, Mörlenbach). Both collagen types are mixed ice-cold at a mass ratio of 1:2 and are dissolved in a dilution medium containing 1 vol part $NaHCO_3$, 1 vol part 10× DMEM and 8 vol parts H_2O, adjusted to pH 9 using NaOH. The final collagen concentrations are adjusted to 0.6 mg/ml, 1.2 mg/ml or 2.4 mg/ml using dilution medium. The pH-value of the final mix is then adjusted to 9 using NaOH. Collagen gels are polymerized for 1 h at 5% CO_2, 37°C.

Cell culture. NK92 cells (ATCC CRL-2407) are cultured at 37 °C and 5% CO_2 in Alpha-MEM medium (Stemcell Technologies) with 15% fetal calf serum, 15% horse serum, 500 IU/ml human IL2-cytokine and 1% penicillin-streptomycin solution (10.000 Units/ml Penicillin, 10.000 µg/ml Streptomcycin).

3D traction force experiments. NK92 cells are suspended in 3 ml ice-cold collagen 1.2 mg/ml solution (66.000 cells/ml), transferred to a 35 mm Nunc dish (Thermo Fischer, Waltham) and polymerized in the incubator (37°C, 5% CO_2) for 1 h. After polymerization, 2 ml of pre-warmed medium are added, and the sample is transferred to an upright laser-scanning confocal microscope (Leica SP5, heated to 37°C with 5% CO_2). To achieve high time resolution we use a resonance scanner (8000 Hz) in combination with a galvo-stage. Image stacks ($123\times123\times123$ µm with a voxel size of $0.24\times0.24\times1$ µm) around individual cells are recorded in brightfield and confocal reflection mode using a 20x water dip-in objective (HCX APO L 20x/1.00 W, Leica, Wetzlar). The acquisition time for an individual image stack is below 10 seconds. Up to four individual cells at different positions are recorded every minute over a period of 24 min.

Bright field microscopy. Differential interference contrast images shown in in Fig. 2h are obtained using an epifluorescence microsope (Leica DMI6000B, Wetzlar) combined with a 63x oil immersion objective (HC PL APO 63x/1,40, Leica, Wetzlar). NK92 cells are imaged during migration through the collagen network with 2 seconds between consecutive images.

Measurement of matrix deformations. Cell-induced matrix deformations are measured from confocal reflection image stacks of the collagen network using 3D particle image velocimetry (OpenPIV) (19). Saenopy offers two options for the detection of matrix deformations. First, matrix deformations can be calculated between a deformed state and a force-free reference state (Fig. 1b top). The reference image stack is typically recorded after drug-induced force relaxation using e.g. high concentrations of cytochalasin D (disrupting the actin cytoskeleton) (15, 16, 29). For fast moving cells, Saenopy offers a second option for obtaining the reference state from a sufficiently long time series of image stacks (Fig. 1b bottom): First, the change in matrix deformations between consecutive image stacks, which correspond to

the time derivative of the matrix deformations, are calculated at each voxel position using OpenPIV (19). We then calculate the cumulative sum of the time derivative at each voxel, which corresponds to the absolute matrix deformation apart from an offset. To remove the offset, we subtract the median deformation at each voxel position, assuming that the median matrix deformations around a fast moving cell tend towards zero, when observed over a prolonged time period. For the NK92 cells in this study, we employ the second option. By comparing a region of the collagen matrix before and after an NK cell has passed through, we confirm that these cells do not permanently remodel the matrix.

For the OpenPIV algorithm, we use a window-size of 12 µm with an overlap of 60% (corresponding to an element size of 4.8 µm). Deformation vectors with low confidence (defined by OpenPIV for a ratio < 1.3 between the global maximum of the image cross correlation divided by the second-highest local maximum value) are ignored. The accuracy with which we can measure matrix deformations with our setup is estimated by imaging collagen gels without cells. We record image stacks at 28 non-overlapping positions in the gel (each 123×123×123 µm), each over a period of 24 min with a time interval of 1 min and a voxel size of 0.24×0.24×1 µm as in the cell experiments. We then compute the deformation field at every voxel position as described above, and the accuracy (noise level) is calculated as the standard deviation σ of all deformation values, separately evaluated in x,y, and z-direction. We obtain values of σ_x=41 nm, σ_y=42 nm, σ_z=99 nm.

Cell tracking. Cell shape and position at each timepoint are extracted from the intensity-projected brightfield image stacks. We compute the local entropy of the band-pass filtered images, subtract the background using regional maxima filtering, binarize the image using Otsu-thresholding (30), and apply binary morphological operations to remove small objects and holes. From the binarized object (which is the segmented cell), we calculate the area, the x,y position (center of mass), and the aspect ratio defined here as the major axis divided by the minor axis of an ellipse fitted to the cell shape. If a cell reaches the edges of the image, this cell is not tracked further.

Correlation analysis. We cross-correlate the time development of cellular contractility, cell speed and cell aspect ratio for all NK92 cells under control conditions (Fig. 2d,f). Since cell velocity and cell forces are calculated from the difference in cell position and matrix deformations between two consecutive image stacks, whereas the aspect ratio is obtained for each single image stack, we linearly interpolate the aspect ratio between two consecutive image stacks before cross-correlation. We then calculate the Spearman rank correlation coefficient between speed and contractility, between speed and aspect ratio, and between contractility and aspect ratio, for time shifts from -7 to +7 min. The error intervals are determined using bootstrapping with a sample-size of 1000.

Force reconstruction. To solve the inverse problem of reconstructing cellular forces $\vec{f}$ from the measured 3D deformation field $\vec{U}^{\text{meas.}}$ (Eq. 5), we use an iterative approach that varies the simulated matrix deformation field $\vec{U}$ with the aim to minimize a target function $L(\vec{U})$. This target function is computed from the difference between the simulated matrix deformations $\vec{U}$ and the measured matrix deformations, $\vec{U}^{\text{meas.}}$, plus a Thikonov regularization term $|\vec{f}(\vec{U})|^2$ (15, 31, 32) to constrain the force field $\vec{f}$:

$$L(\vec{U}) = |\vec{U} - \vec{U}^{\text{meas.}}|^2 + \mathbf{A} \cdot |\vec{f}(\vec{U})|^2 \quad \textbf{(6)}$$

The force field $\vec{f}$ is computed from the simulated deformation field $\vec{U}$ using Eq. 5. The diagonal regularization factor matrix $\mathbf{A}$ has weights that favor large forces (presumably generated by the cell) and penalizes small forces (presumably caused by measurement noise) according to refs (15, 33). At the boundary (surface of the simulated volume) we set the regularization factor to zero (see Section Boundary forces). The index i represents the nodes of the finite element mesh.

$$A_{ii} = \begin{cases} \alpha, & \text{if } |\vec{f_i}| < 1.345 \cdot \text{median}(|\vec{f}|) \\ \alpha \frac{1.345 \cdot \text{median}(|\vec{f}|)}{|\vec{f_i}|}, & \text{if } |\vec{f_i}| \geq 1.345 \cdot \text{median}(|\vec{f}|) \\ 0, & \text{if } i \in \text{Boundary} \end{cases} \quad \textbf{(7)}$$

As $f(\vec{U})$ is non-linear, $L(\vec{U})$ cannot be minimized easily. We apply a Taylor series expansion of the displacement $\vec{U}$ to the first order ($\vec{U} + \Delta\vec{U}$), using the stiffness matrix $\mathbf{K}$ (Eq. 4) (25, 32).

$$L(\vec{U}) = \left(|\vec{U} + \Delta\vec{U} - \vec{U}^{\text{meas.}}|^2 + \mathbf{A} \cdot \left| \left(\vec{f}(\vec{U}) + \mathbf{K}(\vec{U}) \cdot \Delta\vec{U} \right) \right|^2 \right) \quad \textbf{(8)}$$

The $\Delta\vec{U}$ that minimizes this equation satisfies the following normal equation (32).

$$\underbrace{(\mathbf{I} + \mathbf{K}(\vec{U}) \cdot \mathbf{A} \cdot \mathbf{K}(\vec{U}))}_{A_{ij}} \cdot \underbrace{\Delta\vec{u}}_{x_j} = \underbrace{\vec{U}^{\text{meas.}} + \mathbf{K}(\vec{U}) \cdot \mathbf{A} \cdot \vec{f}(\vec{U})}_{b_i} \quad \textbf{(9)}$$

This linear equation (of the form $A_{ij} \cdot x_j = b_i$) is solved using the conjugate gradient method to obtain a value for $\Delta\vec{U}$. Because of the pronounced non-linearity of the problem, for the next iteration cycle we update the simulated deformation field only by a fraction (stepper) of $\Delta\vec{U}$ (typically 0.33):

$$\vec{U}' = \vec{U} + \text{stepper} \cdot \Delta\vec{U}. \quad \textbf{(10)}$$

With the new displacement $\vec{U}'$, the stiffness matrix $\mathbf{K}(\vec{U}')$ (Eq. 4), the nodal forces $\vec{f}(\vec{U}')$ (Eq. 5), and the weight matrix $\mathbf{A}(\vec{f}(\vec{U}'))$ (Eq. 7) are updated, and the linear Taylor expansion (Eq. 9) is solved again. This procedure is iterated until the total energy $E(\vec{U})$ (Eq. 3) of the system converges. Convergence is reached when the standard deviation of $E(\vec{U})$ divided by the mean of $E(\vec{U})$ (Coefficient of Variation) for the last 6 iterations is below a convergence criterion τ (typically 0.01).

From the resulting force vectors $\vec{f_i}$ at all nodes i, we compute the coordinates of the force epicenter $\vec{c}$. To find it, we minimize the magnitude Q of the cross product of the force field

$\vec{f}_i$ with the vectors from the nodes $\vec{r_i}$ pointing to the epicenter coordinates $\vec{c}$: (15, 25).

$$Q = \sum_i \left| \vec{f}_i \times (\vec{r_i} - \vec{c}) \right| \tag{11}$$

We determine the cellular contractility as the sum of the projected forces in the direction of the force epicenter (15, 25):

$$\text{Contractility} = \sum_i \frac{\left\langle \vec{f}_i \cdot (\vec{r_i} - \vec{c})] \right\rangle}{|\vec{r_i} - \vec{c}|} \tag{12}$$

In this study, we perform the force reconstruction of migrating NK92 cells using the regularization parameter $\alpha = 10^{10}$ (Eq. 7), which maximizes contractility and is stable against noise in both, our experimental setup and simulated cells (SI Fig. 9). We interpolate the 3D matrix deformations onto a cubic grid with a grid-size of 4 µm and tesselate cubes into 6 tetrahedra (SI Fig. 10).

Boundary forces. Because the boundary of the simulated, finite-sized volume is fixed, the reconstructed force field contains cell-generated forces from the bulk, as well as distributed counter-forces from the surrounding matrix that appear at the volume boundary. The individual force vectors of the counter-forces are small compared to cell forces. Hence, the small-force penalization scheme (Eq. 7, first and second case) would bundle them into fewer, larger force vectors located in the bulk where they could interfere with cell forces. To avoid this, we set the regularization weights A_{ii} to zero for all tetrahedral mesh nodes at the boundary (surface) of the simulated volume (Eq. 7, third case). Hence, we exclude the surface of the mesh from the regularization cost function so that virtually all counter-forces only appear at the volume boundary and not in the bulk (Fig. 1a). Saenopy can therefore directly sum all the forces in the bulk of the mesh as they are contractile cell forces, without the need to arbitrarily define a maximum radius around the cell center for the summation of forces. This improves robustness and accuracy especially for small stack sizes (Fig. 1c,e).

Simulations of force-generating dipoles and quadrupoles. We simulate the 3-D deformation fields around force-generating dipoles and quadrupoles in a 1.2 mg/ml collagen matrix (Batch A; SI Fig. 1) with the iterative scheme described above, with the following modifications: The displacements at the mesh boundary are set to zero, the forces at the dipole or quadrupole points are given, and the forces in the bulk are set to zero. To simulate contractile dipoles, we add two opposing point forces ($\vec{f}^{\text{ext}}$) with a distance of 15 µm or 30 µm. To simulate contractile quadrupoles, we add 4 inward pointing forces ($\vec{f}^{\text{ext}}$) at the nodes of a regular tetrahedron with an edge length of 15 µm or 30 µm. We now iteratively vary the deformation field until the simulated forces match the imposed force field using the conjugate gradient method as described above. However, instead of the Eq. 9, we solve the following equation:

$$\underbrace{\mathbf{K}(\vec{U})}_{A} \cdot \underbrace{\Delta\vec{U}}_{x} = \underbrace{\vec{f}(\vec{U}) - \vec{f}^{\text{ext.}}}_{b} \tag{13}$$

and update the deformation field $\vec{U}$ after each iteration according to Eq. 10, as well as the the stiffness matrix $\mathbf{K}(\vec{U})$ (Eq. 4) and the nodal forces $\vec{f}(\vec{U})$ (Eq. 5), until the total Energy $E(\vec{U})$ convergences (15, 25).
Point forces are applied to the nearest possible nodes for a grid-size of 4 µm and a stack volume of $(150\,\mu\text{m})^3$. We simulate various contractilities (2 nN–400 nN) with or without added Gaussian noise with a defined standard deviation σ to the deformation field.

Data Availability. The software (Saenopy) and all dependent packages are are available on GitHub as an open-source python package with a graphical user interface (28). Figures are created using the python package Pylustrator (34) and PyVista (35). The data of this study are available upon request from the corresponding author. Rheological measurement of 1.2 mg/ml collagen gels of Batch A were previously published in (36).

Conflict of Interest. The authors declare no competing interests.

Author contribution. Methodology: RG, DB, MC, BF, CM. Software: RG, DB, MC, AB. Rheology: DB, MC, LB, SB. Cell experiments: LB, TC, DB, CV. Data Analysis: DB, LB, CM, RG. Writing: DB, BF, MC, RG.

ACKNOWLEDGEMENTS
This work was funded by grants from the German Science Foundation (FA 336-12/1, TRR-SFB 225 project 326998133 sub-projects A01, B09 and C02), the National Institutes of Health (HL120839), and the Emerging Fields Initiative of the University of Erlangen–Nuremberg (project "Novel Biopolymer Hydrogels for Understanding Complex Tissue Biomechanics"). D.B thanks the ENB Biological Physics program of the University Bayreuth and Ricardo Henriques Laboratory for the use of the latex layout under Creative Commons 4.0 License. We thank Ingo Thievessen for help with DIC imaging and Ronny Reimann for help with the design of the saenopy logo.

Bibliography

1. Micah Dembo and Yu-Li Wang. Stresses at the Cell-to-Substrate Interface during Locomotion of Fibroblasts. Technical report, 1999.
2. Sangyoon J. Han, Youbean Oak, Alex Groisman, and Gaudenz Danuser. Traction microscopy to identify force modulation in subresolution adhesions. *Nature Methods*, 12(7): 653–656, 2015. ISSN 15487105. doi: 10.1038/nmeth.3430.
3. Yunfei Huang, Christoph Schell, Tobias B. Huber, Ahmet Nihat Şimşek, Nils Hersch, Rudolf Merkel, Gerhard Gompper, and Benedikt Sabass. Traction force microscopy with optimized regularization and automated Bayesian parameter selection for comparing cells. *Scientific Reports*, 9(1):1–16, 2019. ISSN 20452322. doi: 10.1038/s41598-018-36896-x.
4. J. P. Butler, I. M. Tolic-Norrelykke, B. Fabry, and J. J. Fredberg. Traction fields, moments, and strain energy that cells exert on their surroundings. *AJP: Cell Physiology*, 2002. ISSN 0363-6143. doi: 10.1152/ajpcell.00270.2001.
5. Martin Bergert, Tobias Lendenmann, Manuel Zündel, Alexander E. Ehret, Daniele Panozzo, Patrizia Richner, David K. Kim, Stephan J.P. Kress, David J. Norris, Olga Sorkine-Hornung, Edoardo Mazza, Dimos Poulikakos, and Aldo Ferrari. Confocal reference free traction force microscopy. *Nature Communications*, 7, 2016. ISSN 20411723. doi: 10.1038/ncomms12814.
6. Benedikt Sabass, Margaret L. Gardel, Clare M. Waterman, and Ulrich S. Schwarz. High resolution traction force microscopy based on experimental and computational advances. *Biophysical Journal*, 94(1):207–220, 2008. ISSN 00063495. doi: 10.1529/biophysj.107.113670.
7. Andreas Bauer, Magdalena Prechová, Lena Fischer, Ingo Thievessen, Martin Gregor, and Ben Fabry. pyTFM: A tool for traction force and monolayer stress microscopy. *PLOS Computational Biology*, 17(6):e1008364, 2021. ISSN 15537358. doi: 10.1371/journal.pcbi.1008364.
8. Cornelis Storm, Jennifer F. Pastore, F. C. MacKintosh, T. C. Lubensky, and Paul A. Janmey. Nonlinear elasticity in biological gels. *Nature*, 435(7039):188–191, 2005. ISSN 00280836. doi: 10.1038/nature03497.1.

9. S. Munster, L. M. Jawerth, B. A. Leslie, J. I. Weitz, B. Fabry, and D. A. Weitz. Strain history dependence of the nonlinear stress response of fibrin and collagen networks. *Proceedings of the National Academy of Sciences*, 110(30):12197–12202, 7 2013. ISSN 0027-8424. doi: 10.1073/pnas.1222787110.
10. D E Discher, P Janmey, and Y L Wang. Tissue cells feel and respond to the stiffness of their substrate 310/5751/1139 [pii] 10.1126/science.1116995. *Science*, 310(5751):1139–1143, 2005.
11. Manuel Gómez-González, Ernest Latorre, Marino Arroyo, and Xavier Trepat. Measuring mechanical stress in living tissues. *Nature Reviews Physics*, 2020. ISSN 25225820. doi: 10.1038/s42254-020-0184-6.
12. Jorge Barrasa-fano, Apeksha Shapeti, Mojtaba Barzegari, and Hans Van Oosterwyck. TFM-LAB : a MATLAB toolbox for 4D traction force microscopy. pages 1–16, 2020.
13. Christian Franck, Stacey A. Maskarinec, David A. Tirrell, and Guruswami Ravichandran. Three-dimensional traction force microscopy: A new tool for quantifying cell-matrix interactions. *PLoS ONE*, 6(3), 2011. ISSN 19326203. doi: 10.1371/journal.pone.0017833.
14. Wesley R. Legant, Jordan S. Miller, Brandon L. Blakely, Daniel M. Cohen, Guy M. Genin, and Christopher S. Chen. Measurement of mechanical tractions exerted by cells in three-dimensional matrices. *Nature Methods*, 7(12):969–971, 2010. ISSN 15487091. doi: 10.1038/nmeth.1531.
15. Julian Steinwachs, Claus Metzner, Kai Skodzek, Nadine Lang, Ingo Thievessen, Christoph Mark, Stefan Münster, Katerina E. Aifantis, and Ben Fabry. Three-dimensional force microscopy of cells in biopolymer networks. *Nature Methods*, 2016. ISSN 15487105. doi: 10.1038/nmeth.3685.
16. M. Cóndor, J. Steinwachs, C. Mark, J. M. García-Aznar, and B. Fabry. Traction force microscopy in 3-dimensional extracellular matrix networks. *Current Protocols in Cell Biology*, 2017. ISSN 19342616. doi: 10.1002/cpcb.24.
17. P Friedl, P B Noble, and K S Zänker. T lymphocyte locomotion in a three-dimensional collagen matrix. Expression and function of cell adhesion molecules. *Journal of immunology (Baltimore, Md. : 1950)*, 154(10):4973–4985, 5 1995. ISSN 0022-1767 (Print).
18. Peter Friedl, Frank Entschladen, Christoph Conrad, Bernd Niggemann, and Kurt S Zänker. CD4+ T lymphocytes migrating in three-dimensional collagen lattices lack focal adhesions and utilize $\beta 1$ integrin-independent strategies for polarization, interaction with collagen fibers and locomotion. *European Journal of Immunology*, 28(8):2331–2343, 1998. ISSN 00142980. doi: 10.1002/(SICI)1521-4141(199808)28:08<2331::AID-IMMU2331>3.0.CO;2-C.
19. Alex Liberzon, Theo Käufer, Andreas Bauer, Peter Vennemann, and Erich Zimmer. OpenPIV/openpiv-python: OpenPIV-Python v0.23.4. 1 2021. doi: 10.5281/ZENODO.4409178.
20. Ingo Thievessen, Nikta Fakhri, Julian Steinwachs, Viola Kraus, R. Scott McIsaac, Liang Gao, Bi Chang Chen, Michelle A. Baird, Michael W. Davidson, Eric Betzig, Rudolf Oldenbourg, Clare M. Waterman, and Ben Fabry. Vinculin is required for cell polarization, migration, and extracellular matrix remodeling in 3D collagen. *FASEB Journal*, 29(11):4555–4567, 2015. ISSN 15306860. doi: 10.1096/fj.14-268235.
21. Mar Cóndor, Christoph Mark, Richard C. Gerum, Nadine C. Grummel, Andreas Bauer, José M. García-Aznar, and Ben Fabry. Breast Cancer Cells Adapt Contractile Forces to Overcome Steric Hindrance. *Biophysical Journal*, 116(7):1305–1312, 2019. ISSN 15420086. doi: 10.1016/j.bpj.2019.02.029.
22. Katarina Wolf, Regina Müller, Stefan Borgmann, Eva B. Bröcker, and Peter Friedl. Amoeboid shape change and contact guidance: T-lymphocyte crawling through fibrillar collagen is independent of matrix remodeling by MMPs and other proteases. *Blood*, 102(9):3262–3269, 2003. ISSN 00064971. doi: 10.1182/blood-2002-12-3791.
23. Cynthia A. Reinhart-King, Micah Dembo, and Daniel A. Hammer. Cell-cell mechanical communication through compliant substrates. *Biophysical Journal*, 95(12):6044–6051, 2008. ISSN 15420086. doi: 10.1529/biophysj.107.127662.
24. Matthew J. Paszek, Nastaran Zahir, Kandice R. Johnson, Johnathon N. Lakins, Gabriela I. Rozenberg, Amit Gefen, Cynthia A. Reinhart-King, Susan S. Margulies, Micah Dembo, David Boettiger, Daniel A. Hammer, and Valerie M. Weaver. Tensional homeostasis and the malignant phenotype. *Cancer Cell*, 8(3):241–254, 2005. ISSN 15356108. doi: 10.1016/j.ccr.2005.08.010.
25. Julian Steinwachs. *Cellular Forces during Migration through Collagen Networks*. PhD thesis, Friedrich-Alexander-Universität Erlangen-Nürnberg, Erlangen, 2015.
26. Delf Kah, Alexander Winterl, Magdalena Přechová, Ulrike Schöler, Werner Schneider, Oliver Friedrich, Martin Gregor, and Ben Fabry. A low-cost uniaxial cell stretcher for six parallel wells. *HardwareX*, 9, 2021. ISSN 24680672. doi: 10.1016/j.ohx.2020.e00162.
27. Uta Faust, Nico Hampe, Wolfgang Rubner, Norbert Kirchgeßner, Sam Safran, Bernd Hoffmann, and Rudolf Merkel. Cyclic stress at mHz frequencies aligns fibroblasts in direction of zero strain. *PLoS ONE*, 6(12), 2011. ISSN 19326203. doi: 10.1371/journal.pone.0028963.
28. Richard Gerum, David Börhinger, and Mar Cóndor. Saenopy Github Project: https://github.com/rgerum/saenopy, 2020.
29. C. Mark, T.J. Grundy, P.L. Strissel, D. Böhringer, N. Grummel, R. Gerum, J. Steinwachs, C.C. Hack, M.W. Beckmann, M. Eckstein, R. Strick, G.M. O'neill, and B. Fabry. Collective forces of tumor spheroids in three-dimensional biopolymer networks. *eLife*, 9, 2020. ISSN 2050084X. doi: 10.7554/eLife.51912.
30. N Otsu. A Threshold Selection Method from Gray-Level Histograms. *IEEE Transactions on Systems, Man, and Cybernetics*, 9(1):62–66, 1979. ISSN 0018-9472. doi: 10.1109/TSMC.1979.4310076.
31. A. N. Tikhonov, A. V. Goncharsky, V. V. Stepanov, and A. G. Yagola. *Numerical Methods for the Solution of Ill-Posed Problems*. Springer Science & Business Media, 1995. doi: 10.1007/978-94-015-8480-7.
32. A N Tikhonov. On the stability of inverse problems. *Proceedings of the USSR Academy of Sciences*, 39:195–198, 1943.
33. Peter J Huber. *Robust statistics. Vol. 523*. John Wiley & Sons, 2004.
34. Richard Gerum. Pylustrator: Code Generation for Reproducible Figures for Publication. *Journal of Open Source Software*, 5(51):1989, 2020. ISSN 2475-9066. doi: 10.21105/joss.01989.
35. C. Sullivan and Alexander Kaszynski. PyVista: 3D plotting and mesh analysis through a streamlined interface for the Visualization Toolkit (VTK). *Journal of Open Source Software*, 4(37):1450, 2019. doi: 10.21105/joss.01450.
36. Luz del Carmen Martínez-Sánchez, Phuong Anh Ngo, Rashmita Pradhan, Lukas-Sebastian Becker, David Boehringer, Despina Soteriou, Marketa Kubankova, Christine Schweitzer, Tatyana Koch, Veronika Thonn, Lena Erkert, Iris Stolzer, Claudia Günther, Christoph Becker, Benno Weigmann, Monika Klewer, Christoph Daniel, Kerstin Amann, Stefan Tenzer, Raja Atreya, Martin Bergo, Cord Brakebusch, Alastair J M Watson, Jochen Guck, Ben Fabry, Imke Atreya, Markus F Neurath, and Rocío López-Posadas. Epithelial RAC1-dependent cytoskeleton dynamics controls cell mechanics, cell shedding and barrier integrity in intestinal inflammation. *Gut*, pages 2021–325520, 2022. ISSN 0017-5749. doi: 10.1136/gutjnl-2021-325520.
37. Nadine R. Lang, Stefan Münster, Claus Metzner, Patrick Krauss, Sebastian Schürmann, Janina Lange, Katerina E. Aifantis, Oliver Friedrich, and Ben Fabry. Estimating the 3D pore size distribution of biopolymer networks from directionally biased data. *Biophysical Journal*, 105(9):1967–1975, 2013. ISSN 00063495. doi: 10.1016/j.bpj.2013.09.038.
38. Patrick Krauss, Claus Metzner, Janina Lange, Nadine Lang, and Ben Fabry. Parameter-free binarization and skeletonization of fiber networks from confocal image stacks. *PLoS ONE*, 7(5):1–8, 2012. ISSN 19326203. doi: 10.1371/journal.pone.0036575.
39. Jui Cheng Yen, Fu Juay Chang, and Shyang Chang. A New Criterion for Automatic Multilevel Thresholding. *IEEE Transactions on Image Processing*, 4(3):370–378, 1995. ISSN 19410042. doi: 10.1109/83.366472.
40. Yoshinobu Sato, Shin Nakajima, Nobuyuki Shiraga, Hideki Atsumi, Shigeyuki Yoshida, Thomas Koller, Guido Gerig, and Ron Kikinis. Three-dimensional multi-scale line filter for segmentation and visualization of curvilinear structures in medical images. *Medical Image Analysis*, 2(2):143–168, 6 1998. ISSN 1361-8415. doi: 10.1016/S1361-8415(98)80009-1.

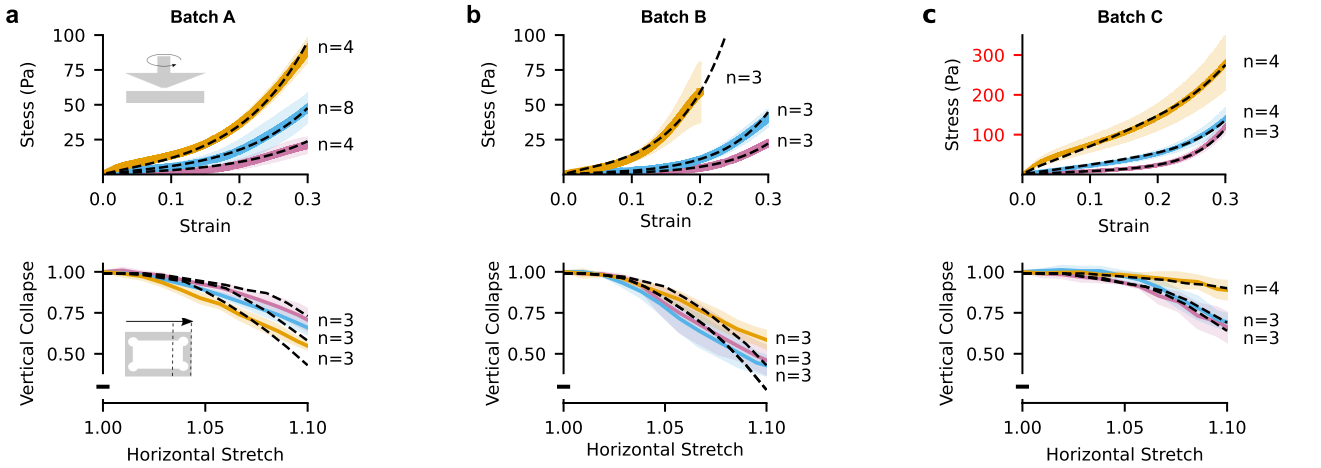

d

	k_0	λ_s	d_s	d_0
Collagen 0.6mg/ml (Batch A)	725	0.0320	0.055	0.0030
Collagen 1.2mg/ml (Batch A)	1449	0.0320	0.055	0.0022
Collagen 2.4mg/ml (Batch A)	2899	0.0320	0.055	0.0015
Collagen 0.6mg/ml (Batch B)	293	0.0230	0.036	0.0013
Collagen 1.2mg/ml (Batch B)	590	0.0230	0.036	0.0013
Collagen 2.4mg/ml (Batch B)	3162	0.0230	0.036	0.0018
Collagen 0.6mg/ml (Batch C)	2045	0.0542	0.027	0.0023
Collagen 1.2mg/ml (Batch C)	6062	0.0804	0.034	0.0025
Collagen 2.4mg/ml (Batch C)	16034	0.0951	0.050	0.0070
Collagen 0.6mg/ml (Steinwachs et al.)	447	0.0075	0.033	0.0008
Collagen 1.2mg/ml (Steinwachs et al.)	1645	0.0075	0.033	0.0008
Collagen 2.4mg/ml (Steinwachs et al.)	5208	0.0075	0.033	0.0008

Collagen 0.6 mg/ml
Collagen 1.2 mg/ml
Collagen 2.4 mg/ml
model

Supplementary Information 1: Collagen rheology and material model

Collagen hydrogels from three different batches (**a**, **b**, **c**) at different concentrations of 0.6 mg/ml (purple), 1.2 mg/ml (blue), and 2.4 mg/ml (orange) are characterized using cone-plate shear-rheological measurements (top) and uniaxial stretch-experiments (bottom) as described in the Methods section of the main text. Solid lines represent the mean, shaded area represent the standard deviation. Dashed lines show the fit of the finite element model to the data. **c**, Model parameters are extracted from the fit for three different batches (Batch A-C). Additionally, previously measured parameters from Steinwachs et al. (15) are given for comparison. For each batch, we performed both individual fits to the data for each concentration separately, or global fits where the parameters λ_s, d_s, and d_0 were the same for all or some of the concentrations. Global fit parameters were preferred if the fit quality was comparable to individual fits, in order to reduce the number of free fit parameters.

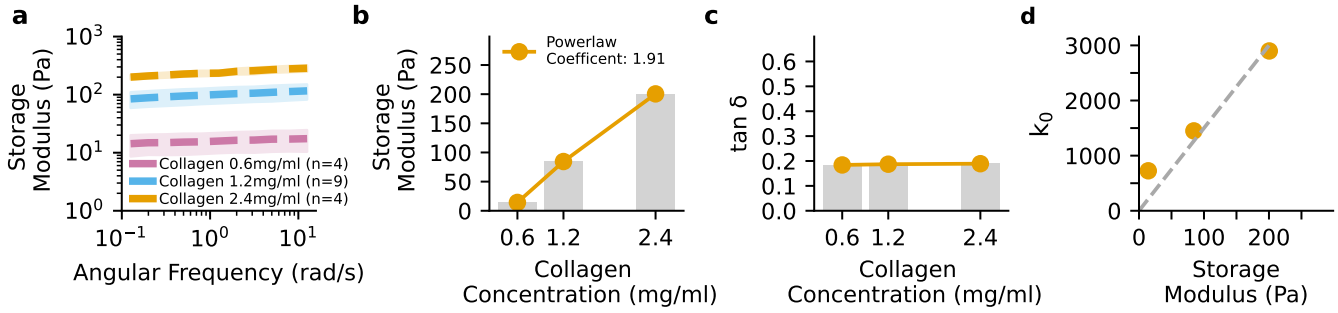

Supplementary Information 2: Small amplitude rheology

a, Storage modulus derived from frequency sweep with a cone-plate rheometer at 1% strain amplitude for different collagen concentration (Batch A, see SI Fig. 1). Dashed lines indicate mean value and shaded area indicate ±sd of individual samples. **b**, Storage modulus (mean value at 0.02 Hz) scales with collagen concentration according to a power-law with exponent of 1.91. **c**, Loss tangent δ (loss modulus G" divided by storage modulus G', averaged from 0.02-2 Hz) remains below 0.2 for all collagen concentrations, indicating predominantly elastic behavior. **d**, The FE model parameter k_0 (indicating the linear stiffness of the collagen fibers) for different collagen concentrations (see SI Fig. 1) increases approximately linearly with the storage modulus G' of the collagen gels (measured at 0.02 Hz at a strain amplitude of 1%). The gray dashed line indicates the predication from continuum mechanics, where $k_0 = 6E$, with Young's modulus $E = G \cdot 2 \cdot (1 + v)$ and Poisson ratio $\nu = 0.25$ for linear elastic, isotropic fiber networks (15). Hence, $k_0 = 15 \cdot G$.

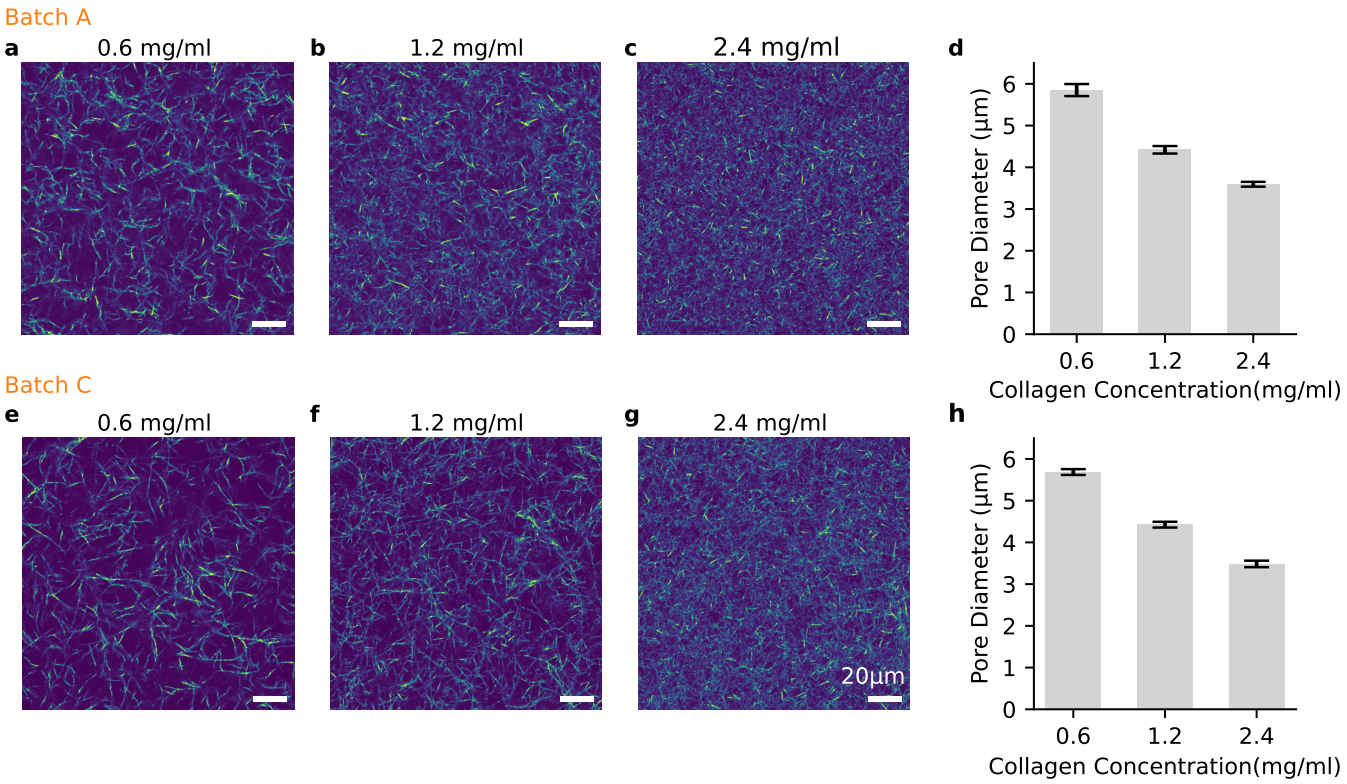

Supplementary Information 3: Microstructure of collagen networks

The collagen fiber structure of two different collagen batches (**a**–**c**: Batch A; **e**–**g**: Batch C) is imaged using confocal reflection microscopy for three different collagen concentrations (imaged volume of 160x160x200 µm with voxel sizes of 0.314x0.314x0.642 µm). Images show a single slice. 3-D pore diameters (from the covering radius transform) are measured as described in (37, 38). The mean pore diameters for each collagen concentration (**d**,**h**) are calculated from 8 different regions within the stacks (80x80x100 µm with 0.314x0.314x0.642 µm). The error bars represent the standard deviation of the mean pore diameter between different regions of the imaged stack.

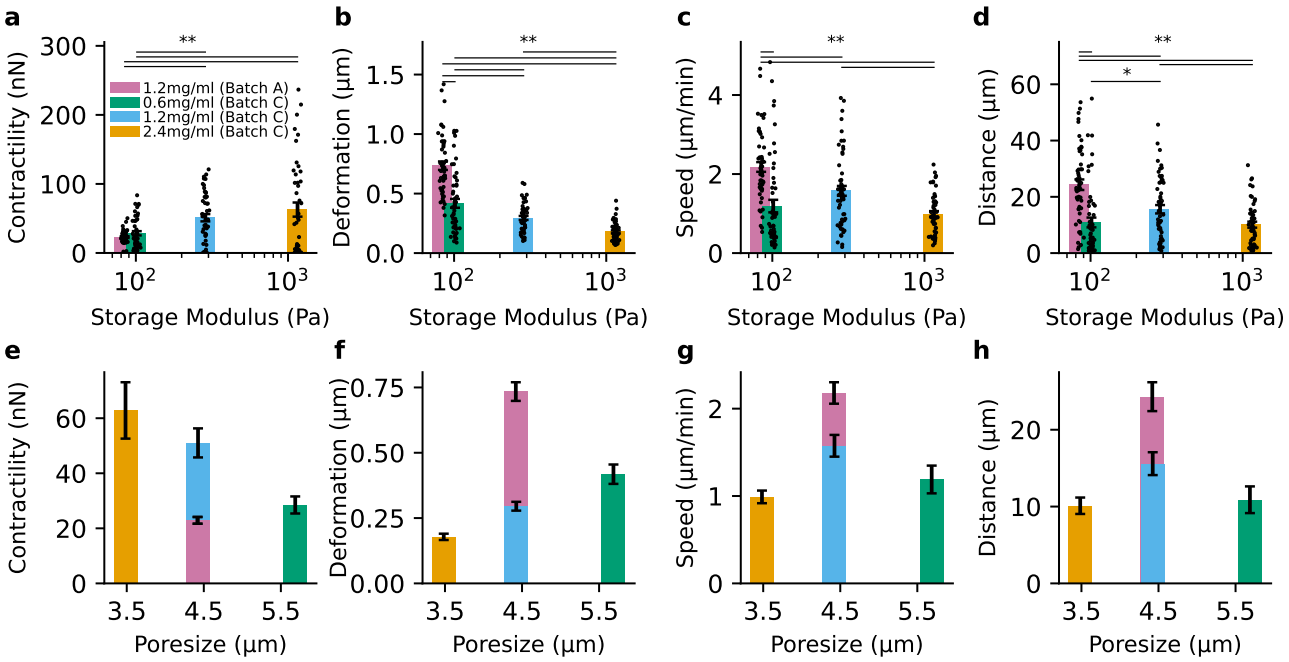

Supplementary Information 4: Immune cell migration and force generation depend on matrix stiffness and pore size

Cell contractility (**a**,**e**), matrix deformations (**b**,**f**), cell speed (**c**,**g**), and cell travelled distance (**d**,**h**) are measured in collagen matrices (0.6 mg/ml, 1.2 mg/ml and 2.4 mg/ml from different collagen batches), resulting in different stiffnesses (**a**–**d**) and pore sizes (**e**–**h**). The storage modulus of different collagen gels is derived from cone-plate shear rheological measurements at 0.02 Hz (1% strain amplitude, see SI Fig. 2), and the pore size is calculated from confocal reflection images (see SI Fig. 3). Black points indicate measurements from individual cells (total of 44–56 cells from three independent experiments), colored bars and error bars indicate mean±se, * indicates $p<0.05$ and ** indicates $p<0.01$ for two-sided t-test. (**a**,**e**), Maximum contractility of each cell during a 24 min measurement period. (**b**,**f**), Maximum of the absolute matrix deformation vector (99% percentile) of each cell during a 24 min measurement period. (**c**,**g**), Mean cell speed during a 24 min measurement period. (**d**,**h**), Maximum Euclidean migration distance from starting position of each cell during a 24 min measurement period. Cell contractility monotonically increases, and matrix deformations monotonically decreases with matrix stiffness. Migration speed and travelled distance show a maximum response at intermediate pore sizes.

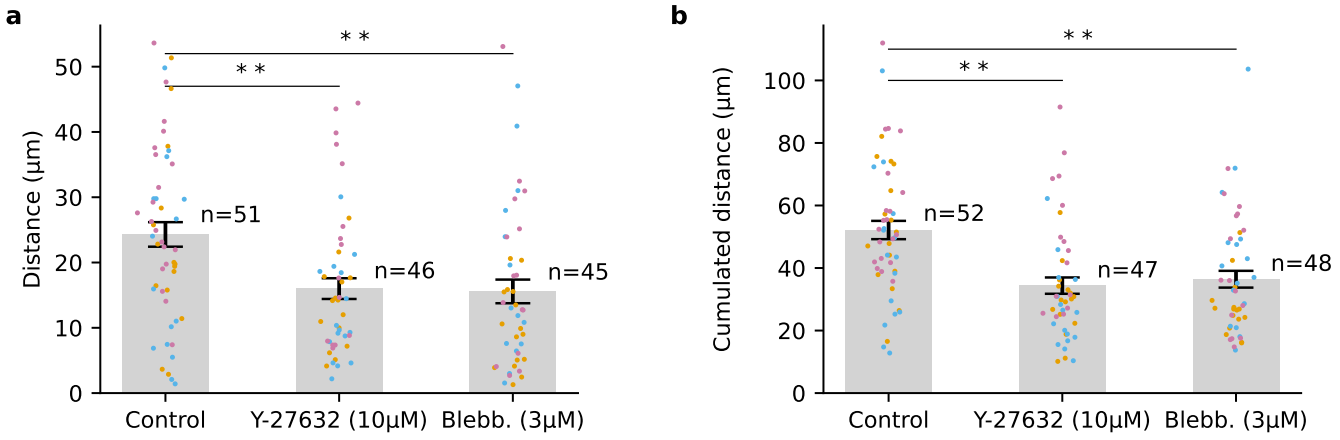

Supplementary Information 5: Migration distance within a 24 min measurement period

a, Maximum Euclidean distance (from starting position) of cell migration within 24 min in 1.2 mg/ml collagen gels. Colored points show data from individual cells (from three independent experiments, indicated by color), bars show mean±se; ** indicates $p<0.01$ for two-sided t-test. **b**, Path length of cell trajectory within 24 min in 1.2 mg/ml collagen gels. Time interval between individual frames is dt=1 min.

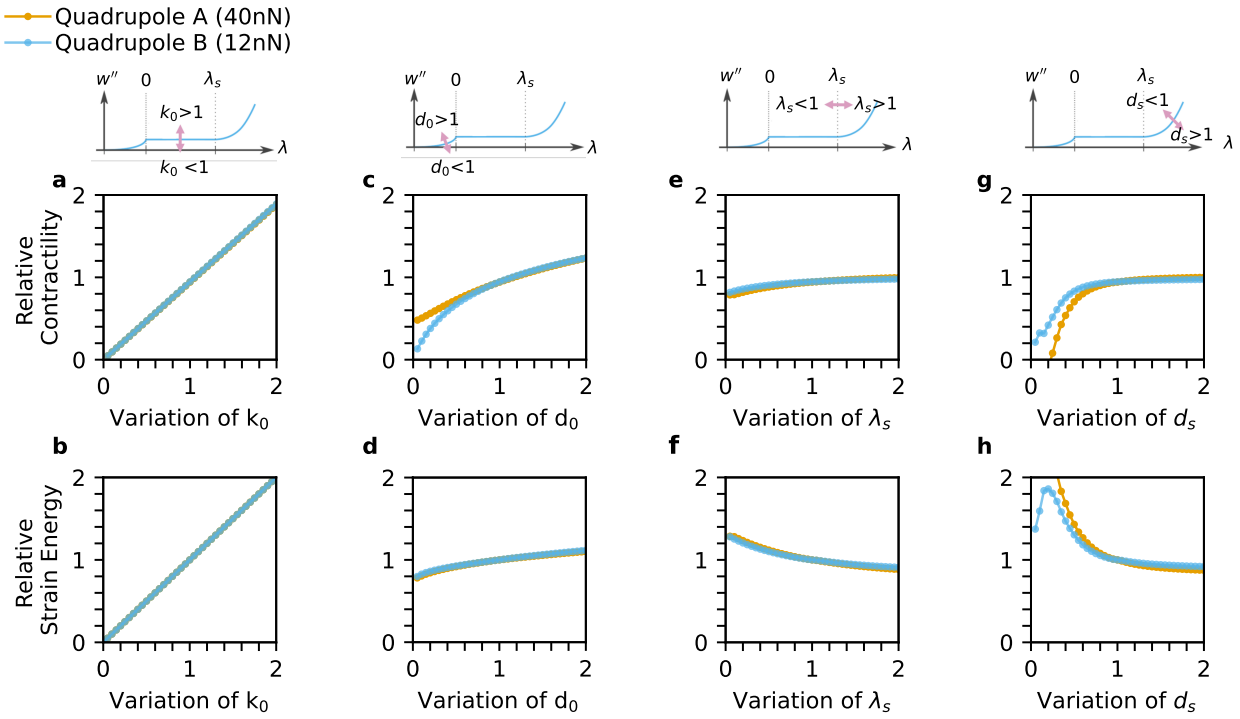

Supplementary Information 6: Influence of material parameters on force reconstruction for differently contractile quadrupoles

3-D matrix deformation fields are simulated for quadrupoles with a total contractile force of 40 nN (orange) or 12 nN (blue) that contract in a 1.2 mg/ml collagen gel (Batch A, SI Fig. 1). We then evaluate how the reconstructed cell contractility and strain energy are affected by variations of the material parameters. Specifically, we alter the four material parameters (linear stiffness k_0 (**a,b**), buckling coefficient d_0 (**c,d**), characteristic strain λ_s (**e,f**), and stiffening coefficient d_s) (**g,h**) individually with respect to the original material values used for computing the deformation field. Results are expressed as reconstructed contractility relative to ground truth of 40 nN or 12 nN, respectively, and as strain energy relative to the ground truth of the strain energy obtained for the original material values. We find that increasing linear stiffness k_0 results in a proportional increase of relative contractility (**a**) and relative strain energy (**b**) regardless of total quadrupole contractility. Increasing the buckling coefficient d_0 results in a less than proportional increase of contractility (**c**) and strain energy (**d**), except for very low values where the contractility of the 12 nN quadrupole depends more strongly on d_0. Increasing the linear strain range λ_s results in an weak increase of contractility (**e**) and a weak decrease in strain energy (**f**). Increasing the stiffening coefficient d_s results in a increase of contractility (**g**) and a decrease in strain energy (**h**). At low values of d_s, the dependency of the 40 nN quadrupole is more pronounced. In general, we find that the contractility and strain energy for differently contractile quadrupoles change proportionally, which implies that relative changes in contractility can be correctly inferred even with the incorrect material model, except for material parameters that cause extremely non-linear material behavior (very low d_0 and d_s).

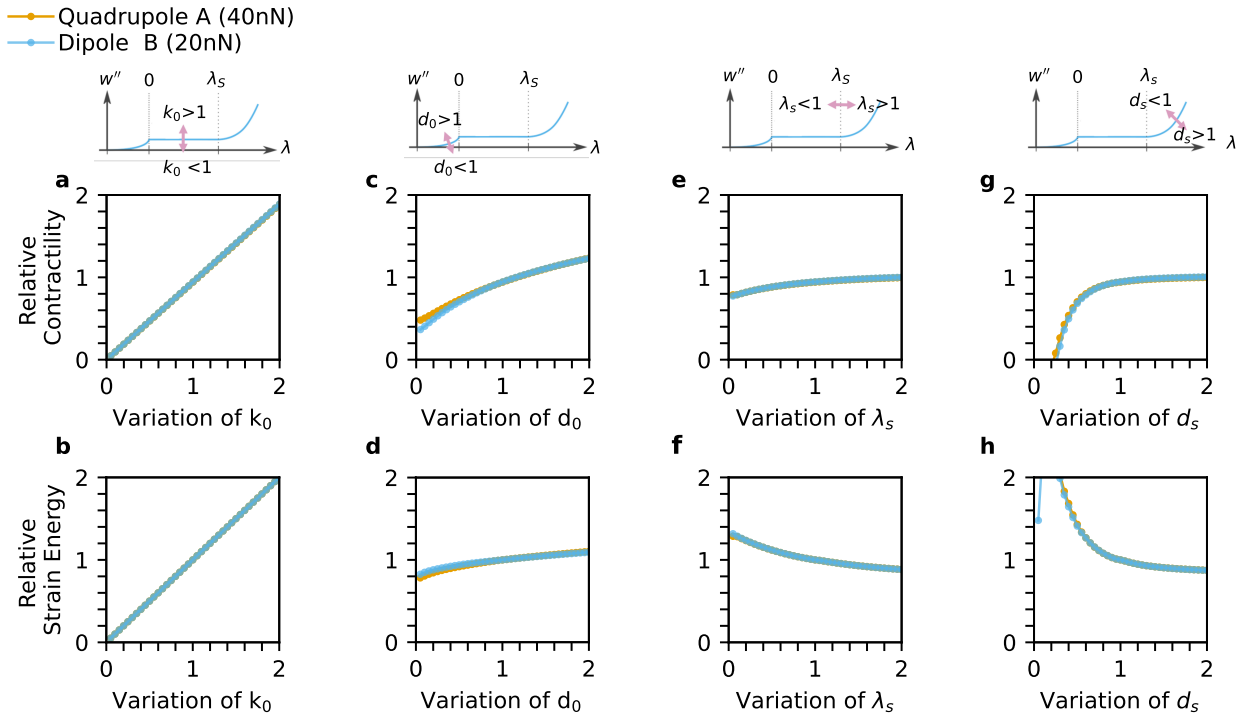

Supplementary Information 7: Influence of material parameters on force reconstruction for dipoles versus quadrupoles

3-D matrix deformation fields are simulated for a quadrupole with a total contractile force of 40 nN (orange) and a dipole with a total contractile force 20 nN (blue) that contract in a 1.2 mg/ml collagen gel (Batch A, SI Fig. 1). We then evaluate how the reconstructed cell contractility and strain energy are affected by variations of the material parameters. As in SI Fig. 6, we alter the four material parameters (linear stiffness k_0 (**a,b**), buckling coefficient d_0 (**c,d**), characteristic strain λ_s (**e,f**), and stiffening coefficient d_s) (**g,h**) individually with respect to the original material values used for computing the deformation field. Results are expressed as reconstructed contractility relative to ground truth of 40 nN or 20 nN, respectively, and as strain energy relative to the ground truth of the strain energy obtained for the original material values. We find that increasing linear stiffness k_0 result in a proportional increase of relative contractility (**a**) and relative strain energy (**b**) regardless of total contractility. Increasing the buckling coefficient d_0 results in a less than proportional increase of contractility (**c**) and strain energy (**d**). Increasing the linear strain range λ_s results in an weak increase of contractility (**e**) and a weak decrease in strain energy (**f**). Increasing the stiffening coefficient d_s results in a increase of contractility (**g**) and a decrease in strain energy (**h**). In general, we find that the contractility and strain energy for contractile quadrupoles and dipoles change proportionally, which implies that spatial arrangements of the monopole forces can be correctly inferred even with the incorrect material model.

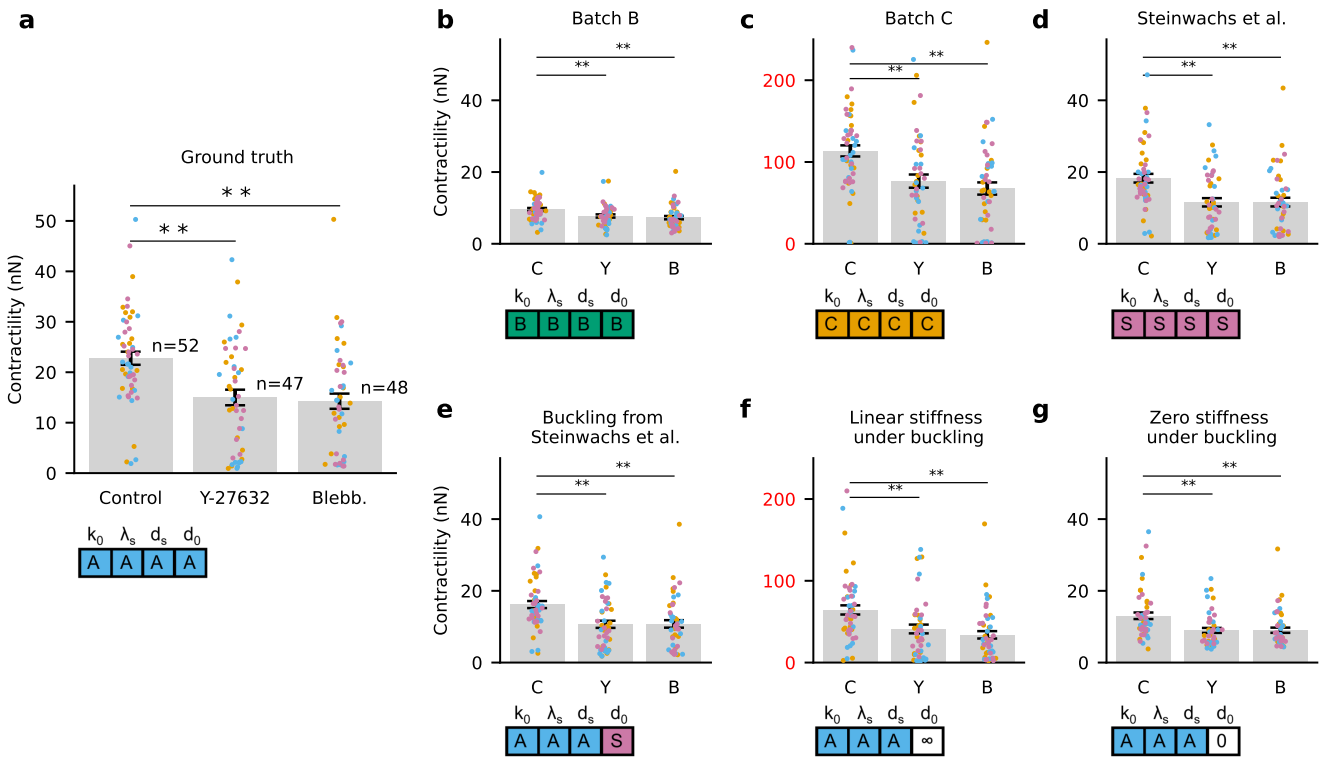

Supplementary Information 8: Influence of material parameters on force reconstruction for immune cells

a, Ground truth of contractile forces (same data as shown in Fig. 2) for cells measured in 1.2 mg/ml collagen of Batch A. Force reconstruction is performed with the correct material model (for Batch A, see SI Fig. 1). (**b–g**), Force reconstruction for the same data is performed with incorrect material models from different collagen batches: (**b**) for Batch B, (**b**) for Batch C, (**d**) for values reported in Steinwachs et al. (15), (**e**) for Batch A but with the incorrect buckling coefficient from Steinwachs et al. (15), (**f**) for Batch A but with an infinite buckling coefficient (corresponding to a linear behavior of the collagen fibers under compression), (**g**) for Batch A but with a zero buckling coefficient (corresponding to zero fiber stiffness under compression). The largest errors (highlighted in red axis labels) are observed when fiber buckling is ignored (**f**) or when the linear stiffness greatly differs from the correct value (**c**). Despite the choice of incorrect material models for force reconstruction, differences between control and drug treatment conditions remain statistically significant ($p<0.01$) in all cases. Points indicate data from individual cells, with independent experiments highlighted by different colors. Bars show mean±sd; ** indicates $p<0.01$ for two-sided t-test.

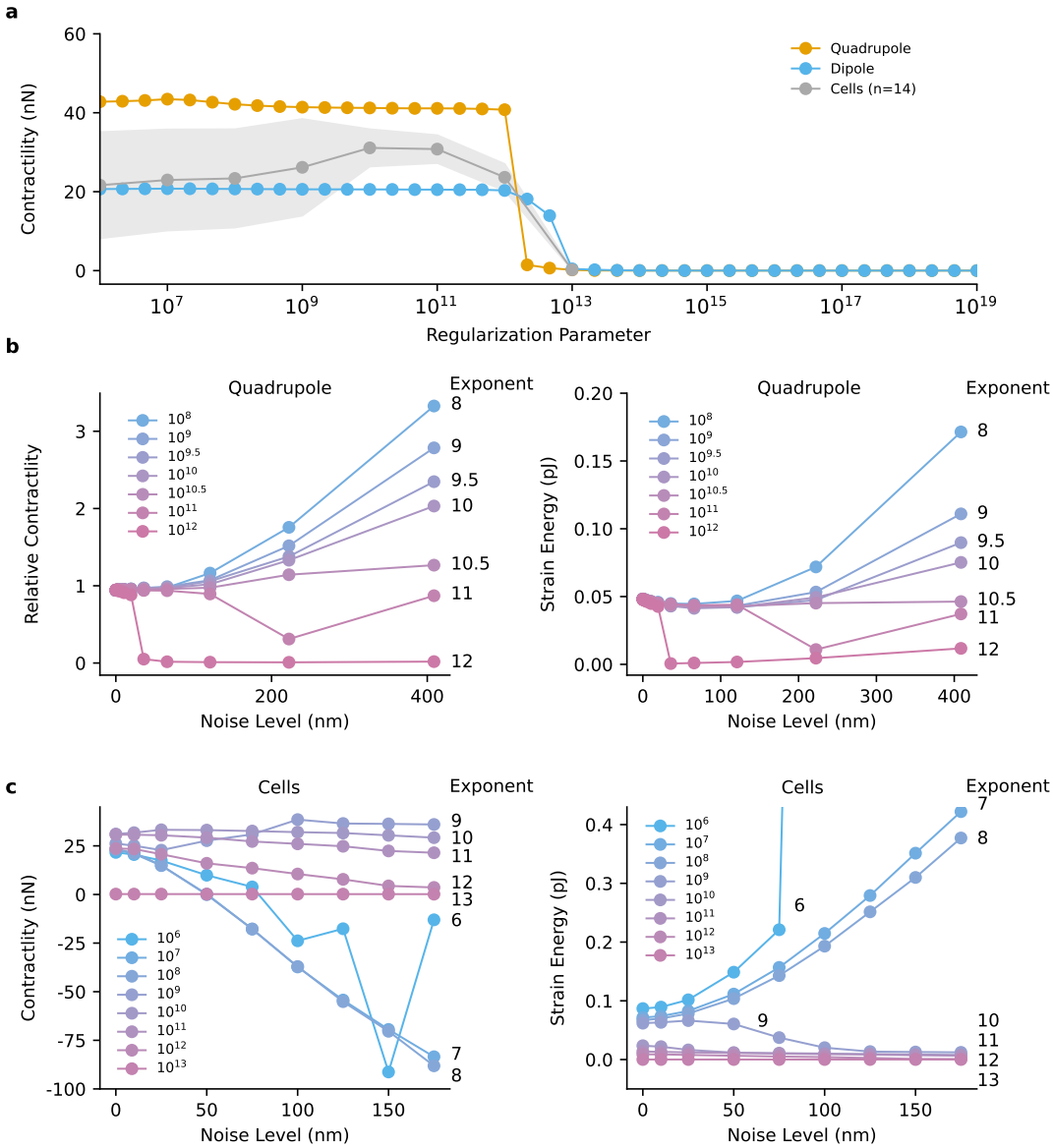

Supplementary Information 9: Influence of the regularization parameter on force reconstruction

a, Contractility of a simulated dipole (20 nN) without noise, simulated quadrupole (40 nN) without noise, and randomly selected contractile NK92 cells (n=14, mean±se). Force reconstruction is performed with different values for the regularization parameter α. We find that a regularization parameter above 10^{13} removes most force components. For simulated force dipoles or quadrupoles in the absence of noise, a regularization parameter $< 10^{12}$ gives the correct value. For (noisy) cell measurements in our setup, a regularization parameter around 10^{10} results in a maximum force. Lower regularization parameter can both underestimate and overestimate total cell contractility as more and more random noise forces appear, resulting in an increased variance between different cells. **b**, Contractility (left) and strain energy (right) for a simulated quadrupole (40 nN) for different values of the regularization parameter and different noise levels (Gaussian noise with a specified standard deviation added to the deformation field around the quadrupole). Contractility (left) is normalized to 40 nN. In our setup, a regularization parameter between 10^{10} and 10^{11} is robust against high noise levels. Reconstructed forces are increasingly overestimated for regularization parameters below $< 10^{10}$ and underestimated for regularization parameters above 10^{11}. **c**, Contractility (left) and strain energy (right) contractile NK92 cells (n = 14, standard errors are not shown for clarity). Gaussian noise on top of the experimental noise level (σ_x=41 nm, σ_y=42 nm, σ_z=99 nm) is added to the deformation field (as in **b**). Reconstructed forces are largely unaffected by additional noise for regularization parameter between 10^9 and 10^{11}. Larger and smaller regularization parameters both lead to increasingly erratic behavior of reconstructed forces for higher noise levels. The strain energy increases with noise for regularization parameter below 10^9. Taken these results together, a choice of around 10^{10} for the regularization parameter results in the most accurate and robust force estimate in our setup.

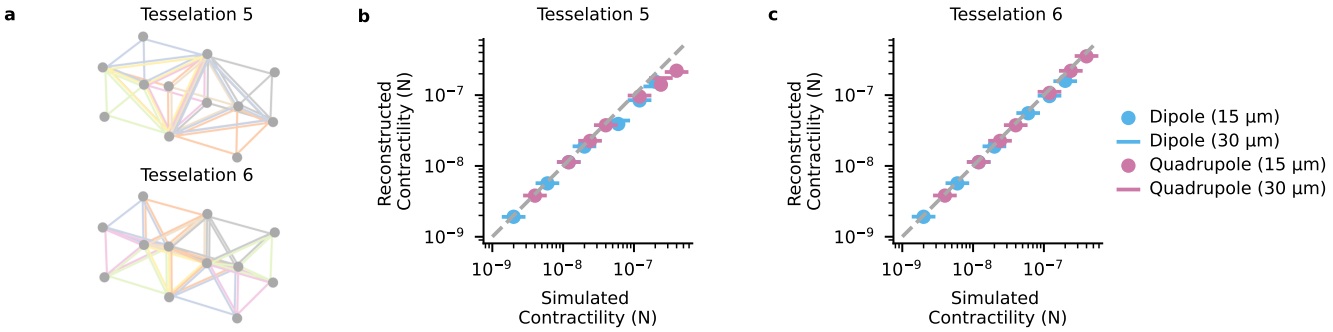

Supplementary Information 10: Effect of different tessellation approaches for finite-element meshes

a, Cubical meshes are tessellated into either 5 tetrahedra (not of equal volume) or 6 tetrahedra (of equal volume). **b**, Reconstructed contractility (for 5 tetrahedra sub-tessellation) for differently contractile dipoles (two force monopoles 15 µm or 30 µm apart) and quadrupoles (force monopoles at the vertices of a regular tetrahedron with an edge length of 15 µm or 30 µm). For total contractilities above 50 nN, the reconstructed forces become increasingly underestimated. **c**, same as in (**b**) for 6 tetrahedra sub-tessellation. In contrast to a 5 tetrahedra sub-tessellation, forces are correctly reconstructed also for higher contractilities (**c**).

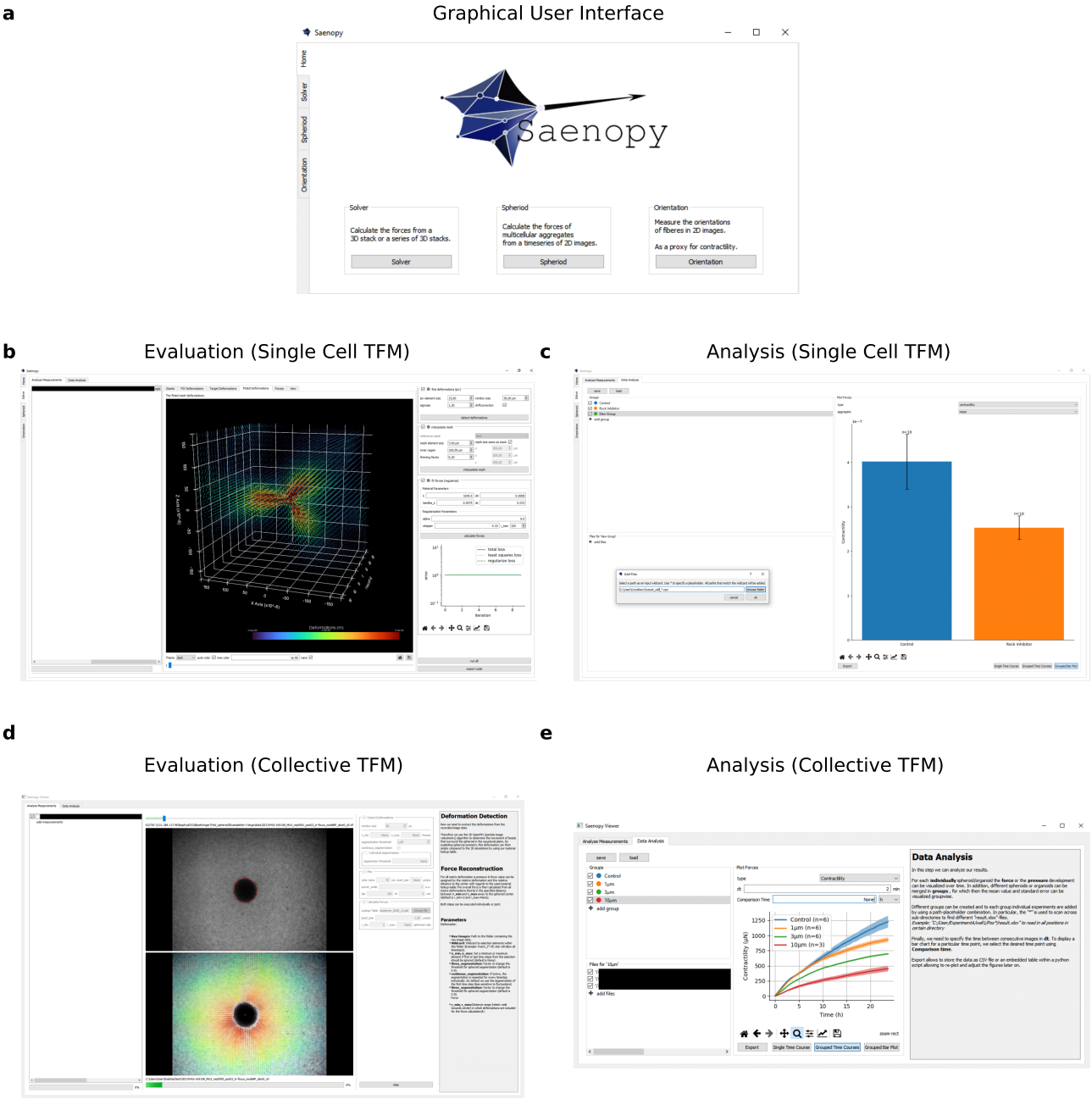

Supplementary Information 11: Graphical User Interface

Graphical User Interface for the open-source python package Saenopy (28) that allows to conduct dynamical or static traction force measurements of single cells (**a**,**b**) or of multicellular aggregates (spheroids, organoids, **d**; previously described in (29, 36)). Results can be evaluated and visualized individually or for grouped experiments (**c**,**e**).

Supplementary Information 12: Video of migrating NK92 cell through collagen (brightfield & confocal reflection)

Intensity projected image stacks of a migrating NK92 cell through 1.2 mg/ml collagen hydrogels (stack-size of 123×123×123 µm with a voxel-size of 0.24×0.24×1 µm) recorded every minute. The cell shows a short phase of high contractility around 4 min. Left: Brightfield image. Right: Confocal reflection image. Projected matrix deformations are indicated by colored arrows. Scale-bar is 20 µm. For better visualization of matrix deformations, the video is followed by a forward-backward sequence of consecutive images during a phase with high contractility.

Supplementary Information 13: Video of migrating NK92 cell through collagen (DIC)

Differential contrast images of a migrating NK92 cell through 1.2 mg/ml collagen hydrogels. Timestep between consecutive frames is 2 seconds. The focus has been adjusted manually during the recording. For better visualization of matrix deformations, the video is followed by a forward-backward sequence of consecutive images during a phase with high contractility.

Supplementary Information 14: Video of migrating NK92 cell through collagen (3D representation)

3D representation of a NK92 cell (green) migrating through dense constrictions in a 1.2 mg/ml collagen hydrogel (brown). The cell is imaged using calcein staining (2 µM Calcein AM, Thermo Fisher Scientific, USA) and segmented using Yen thresholding (39). Collagen fibers are imaged using confocal reflection microscopy. Images are Sato-filtered for ridge detection, highlighting the fiber structure (40). The transparency of the cell- and collagen image-stacks are determined by the intensity values according to a sigmoidal transfer function. Recorded stack-size is 123x123x40 µm with a voxelsize of 0.24x0.24x1.5 µm. Time between consecutive image stacks is 1 min. Matrix deformations are indicated by colored arrows. For better visualization of matrix deformations, the video is followed by a forward-backward sequence of consecutive images during a phase with high contractility.

Supplementary Information 15: Video of migrating NK92 cell through collagen (3D representation)

3D representation of a NK92 cell (green) migrating through dense constrictions in a 1.2 mg/ml collagen hydrogel (brown). The cell is imaged using calcein staining (2 µM Calcein AM, Thermo Fisher Scientific, USA) and segmented using Yen thresholding (39). Collagen fibers are imaged using confocal reflection microscopy. Images are Sato-filtered for ridge detection, highlighting the fiber structure (40). The transparency of the cell- and collagen image-stacks are determined by the intensity values according to a sigmoidal transfer function. Recorded stack-size is 123x123x40 µm with a voxelsize of 0.24x0.24x1.5 µm. Time between consecutive image stacks is 1 min. Matrix deformations are indicated by colored arrows.